

Hyperfine structure of the $(3s3d)^3D_J$ manifold of $^{25}\text{Mg I}$

N. K. Kj oller,^{1,*} S. G. Porsev,^{2,3} P. G. Westergaard,^{1,†} N. Andersen,¹ and J. W. Thomsen^{1,‡}

¹*The Niels Bohr Institute, University of Copenhagen, Blegdamsvej 17, DK-2100 Copenhagen, Denmark*

²*Department of Physics and Astronomy, University of Delaware, Newark, Delaware 19716, USA*

³*Petersburg Nuclear Physics Institute, Gatchina, Leningrad District 188300, Russia*

(Received 8 July 2014; published 26 March 2015)

Based on spectroscopy of the $(3s3p)^3P_0$ - $(3s3d)^3D_1$ Mg I transitions for the stable isotopes ^{24}Mg ($I = 0$), ^{25}Mg ($I = 5/2$), and ^{26}Mg ($I = 0$) we report measurements of the ^{25}Mg $(3s3d)^3D_J$ hyperfine coefficients $A(^3D_1) = 141 \pm 7$, $A(^3D_2) = -59 \pm 6$, and $A(^3D_3) = -97 \pm 3$ MHz. We find the hyperfine coefficients in agreement with state-of-the-art theoretical predictions presented here giving $A(^3D_1) = 143.3 \pm 1.4$, $A(^3D_2) = -48.3 \pm 0.5$, and $A(^3D_3) = -96 \pm 1$ MHz. We also report measurements of the isotope shifts for the investigated transitions $\Delta^{24-25} = 6 \pm 9$ and $\Delta^{24-26} = 59.7 \pm 0.5$ MHz, significantly reducing the uncertainty compared to previous measurements.

DOI: [10.1103/PhysRevA.91.032515](https://doi.org/10.1103/PhysRevA.91.032515)

PACS number(s): 31.15.ac, 32.10.Fn, 32.70.-n

I. INTRODUCTION

The physics of cold alkaline-earth-metal atoms has experienced tremendous progress during the past decades. One of the reasons is the rich energy-level structure associated with the two electron systems. This allows for efficient cooling and trapping of a large number of atoms as well as offering ultranarrow intercombination line transitions well suited for the realization of, e.g., low-temperature samples, optical atomic clocks, precision measurements, quantum degenerate gases, and quantum information processing [1–4].

Among the alkaline-earth-metal atoms explored for optical clocks the magnesium atom plays a special role. Together with mercury, magnesium is the neutral two-valence electron atom with the lowest sensitivity to black body radiation compared to, for example, strontium and ytterbium. These finite temperature effects are currently limiting state-of-the-art optical atomic clocks [3–6]. In addition, second stage cooling using the $(3s^2)^1S_0$ - $(3s3p)^3P_1$ intercombination line has proven difficult for magnesium atoms. An alternative approach where magnesium atoms are transferred to metastable 3P_J states followed by multiline cooling on the 3P_J - 3D_J manifold seems promising [2] as it opens for efficient transfer of atoms to an optical lattice operated at the magic wavelength followed by clock operation.

In this paper we present spectroscopic data for the $(3s3p)^3P_0$ - $(3s3d)^3D_1$ 383-nm transition highlighted in Fig. 1 and compare to state-of-the-art theoretical calculations. Magnesium has three stable isotopes, two bosonic and one fermionic isotope, ^{24}Mg ($I = 0$), ^{25}Mg ($I = 5/2$), and ^{26}Mg ($I = 0$), so spectroscopy involves both fine and hyperfine structure. Pioneering measurements reported in Ref. [9] revealed a spectroscopic structure for the fermionic isotope that deviated significantly from the fine structure energy-level diagram presented in Fig. 1 with the hyperfine structure (hfs) added successively. This approach is troublesome as also pointed out in Ref. [9] since the fine and the hyperfine splittings

are of the same order of magnitude in this case. In this paper we explain the nature of the spectra by including fine structure and hfs on an equal footing and diagonalizing the corresponding Hamiltonian. This allows us to extract experimentally the ^{25}Mg $(3s3d)^3D_J$ hfs coefficients for comparison with state-of-the-art theoretical predictions. In addition, we measured the isotope shifts of the $(3s3p)^3P_0$ - $(3s3d)^3D_1$ Mg I transitions for ^{24}Mg , ^{25}Mg , and ^{26}Mg .

II. THEORY OF MEASUREMENT

The comparable fine and hyperfine splitting of the fermionic ^{25}Mg $(3s3d)^3D$ levels entails that the fine structure and hfs are included in the Hamiltonian on an equal footing. Neglecting contributions from interactions of the atom with an external magnetic field we arrive at the Hamiltonian,

$$H = H_F + H_{\text{HF}}, \quad (1)$$

consisting of the fine structure Hamiltonian H_F and the hyperfine counterpart H_{HF} . Hyperfine levels of the same F 's but different J 's will thus mix when the combined Hamiltonian is diagonalized. As a result, the states $|^3D_J, F\rangle$ having $F = 3/2, 5/2, 7/2$ mix to form nine eigenstates of H , all with nonzero projections onto states with $J = 1$.

Diagonalization of the Hamiltonian proceeds in a standard way. For H_F we assume the fine structure splittings of the triplet D states to be known from previous experiments [10], whereas the hfs of ^{25}Mg 3D_J is not known. The hfs coupling H_{HF} due to nuclear multipole moments may be represented as a scalar product of two tensors of rank k ,

$$H_{\text{HF}} = \sum_{k=1}^{\infty} \mathbf{N}^{(k)} \cdot \mathbf{T}^{(k)}. \quad (2)$$

Here $\mathbf{N}^{(k)}$ and $\mathbf{T}^{(k)}$ act in the space of nuclear and electronic coordinates, respectively. Using this expression the matrix elements of H_{HF} may be written as [11]

$$\begin{aligned} \langle ^3D_J, F | H_{\text{HF}} | ^3D_{J'}, F \rangle &= (-1)^{I+J+F} \sum_k \langle I || N^{(k)} || I \rangle \\ &\times \langle ^3D_J || T^{(k)} || ^3D_{J'} \rangle \begin{Bmatrix} I & I & k \\ J & J' & F \end{Bmatrix}, \quad (3) \end{aligned}$$

*Present address: DTU Fotonik, Technical University of Denmark, Building 343,  rsteds Plads, DK-2800 Kgs. Lyngby, Denmark.

†Present address: Danish Fundamental Metrology, Matematiktorvet 307, DK-2800 Kgs. Lyngby, Denmark.

‡jw@fys.ku.dk

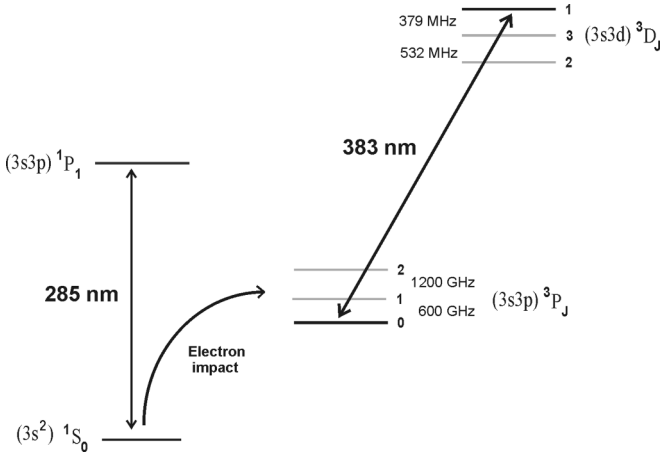


FIG. 1. Energy levels involved in spectroscopy of metastable magnesium $(3s3p)^3P_0$ - $(3s3d)^3D_1$. Atoms are transferred to the $(3s3p)^3P_J$ states via electron impact. The resonance transition at 285 nm is used to determine the absolute fraction of atoms transferred to the metastable 3P_J states [7,8].

where $\langle I || N^{(k)} || I \rangle$ and $\langle ^3D_J || T^{(k)} || ^3D_{J'} \rangle$ denote the reduced matrix elements of $\mathbf{N}^{(k)}$ and $\mathbf{T}^{(k)}$, respectively. In the following we consider only the first term in the series. Due to significant mixing, the hyperfine levels are not described completely by the hyperfine magnetic dipole (A) constants alone. By including the off-diagonal matrix elements of $\mathbf{T}^{(1)}$ we have been able to explain the additional transitions observed in the 3P_0 - 3D_1 spectrum, and as a result we have extracted all 14×14 matrix elements of the hfs Hamiltonian from our data. In Appendix A we show that H_{HF} can be completely characterized in terms of five linearly independent reduced matrix elements of $\mathbf{T}^{(1)}$ out of 3×3 possible. In Appendix B we develop a model relating these five matrix elements as well as the isotope shifts for ^{24}Mg , ^{25}Mg , and ^{26}Mg to the line shape of the observed spectra. In the following we describe first the theoretical predictions, then we apply the model developed in Appendix B to determine experimentally the five independent reduced matrix elements of $\mathbf{T}^{(1)}$ as they are sufficient to determine all matrix elements of H_{HF} .

III. METHOD OF CALCULATION

Spectroscopic properties of Mg I were calculated in a recent paper [12]. In this paper we use the same method of calculation. For this reason we only briefly recapitulate the main features of this approach. We start from the solution of the Dirac-Fock (DF) equations,

$$H_0 \psi_c = \varepsilon_c \psi_c, \quad (4)$$

where H_0 is the relativistic DF Hamiltonian [13,14] and ψ_c and ε_c are single-electron wave functions and energies, respectively.

We treat Mg as a two-valence electron atom. An initial self-consistency procedure is carried out for the $[1s^2 2s^2 2p^6]$ closed core, and the $3s$, $3p$, $3d$, $4s$, $4p$, and $4d$ orbitals are formed in the field of the frozen core (the V^{N-2} approximation) [12,15]. The dominant part of the Breit interaction is also included self-consistently [16]. We use the B -spline basis set formed

in a spherical cavity with a radius of 60 a.u., consisting of 35 orbitals for each partial wave up to $l = 5$. All five partial waves with the orbitals having principal quantum numbers $n \leq 23$ are involved in forming the configuration space. We construct the set of configurations by single and double excitations of the electrons from the main configuration $3s^2$ to the $4s$ - $23s$, $3p$ - $23p$, $3d$ - $23d$, $4f$ - $23f$, and $5g$ - $23g$ orbitals. As discussed in Ref. [12] such a configuration space is numerically complete.

The wave functions and energy levels are found by solving the multiparticle relativistic equation for two-valence electrons [17],

$$H_{\text{eff}}(E_n) \Phi_n = E_n \Phi_n, \quad (5)$$

where the effective Hamiltonian is defined as

$$H_{\text{eff}}(E) = H_{\text{FC}} + \Sigma(E), \quad (6)$$

with H_{FC} being the Hamiltonian in the frozen-core approximation. The energy-dependent operator $\Sigma(E)$ accounts for virtual excitations of the core electrons. It is constructed using the CI+MBPT approach combining configuration-interaction (CI) and second-order many-body perturbation theory (MBPT) [13] and the CI+all-order approach combining CI with linearized coupled cluster single-double method [14]. The construction of the effective Hamiltonian in the CI+MBPT and CI+all-order approximations was described in detail in Refs. [13,14].

Using the wave functions of the 3D_J states obtained by solving Eqs. (5) and (6) the matrix elements of operator $\mathbf{T}^{(1)}$ can be found theoretically. We calculate $\langle ^3D_J || T^{(1)} || ^3D_{J'} \rangle$ in the frame of both the CI+MBPT and the CI+all-order methods. As we show in Appendix A, the diagonal matrix elements $\langle ^3D_J || T^{(1)} || ^3D_J \rangle$ are connected by a simple formula with magnetic dipole hfs constants.

To estimate the accuracy of calculation we present in Table I the hfs constants of the low-lying states obtained in the CI+MBPT and CI+all-order approximations. In calculating these quantities the random-phase approximation (RPA) corrections were also included. As seen from the table, the difference between the hfs constants obtained at the CI+MBPT and CI+all-order stages is less than 0.1%, i.e., the high-order corrections are very small. Additional

TABLE I. Theoretical hfs constants of the even-parity $3s3d^3D_J$ states and the odd-parity $3s3p^3P_{1,2}$ states obtained in the CI+MBPT+RPA and CI+all-order+RPA approximations are given in the columns labeled “CI+MBPT” and “CI+all,” correspondingly. The rounded CI+all values, given in the column labeled “Final,” are treated as final theoretical results. All values are in megahertz. The uncertainties on the final digits are given in parentheses for the experimental values.

	CI+MBPT	CI+all	Final	Expt.
$A(^3D_1)$	143.31	143.29	143.3 ± 1.4	
$A(^3D_2)$	-48.34	-48.31	-48.3 ± 0.5	
$A(^3D_3)$	-95.92	-95.92	-96 ± 1	
$A(^3P_1)$	-144.14	-144.11	-144.1 ± 1.4	$144.977(5)^a$
$A(^3P_2)$	-128.26	-128.23	-128.2 ± 1.3	$-128.445(5)^a$

^aReference [7].

corrections beyond random-phase approximation, such as the core-Brueckner, two-particle corrections, structural radiation, and normalization corrections (see, e.g., Ref. [18] for more details) contribute according to our estimate at the level of a few tenths percent. As an additional test of the accuracy we have calculated the hfs constants for the $3s3p^3P_1$ and $3s3p^3P_2$ states and found agreement with the experimental results [7] at the levels of 0.6% and 0.2%, correspondingly (see Table I). Based on these considerations we conservatively assign 1% uncertainty to the theoretical values. The CI + all-order + RPA values are treated as final theoretical results. Experimental determination of the hfs constants of the $3s3d^3D_J$ states will be discussed in detail in the following sections.

IV. EXPERIMENTAL SETUP

Figure 2 shows the experimental setup used. The magnesium oven is operated at around 520 °C and produces a flux of about 10^{13} at./s. Electron impact produces metastable atoms and initiates a discharge which runs at a stable current of about 1 A comparable to the setup described in Ref. [8]. By exciting the magnesium beam with resonant 285-nm light (not shown in Fig. 2) 20 cm downstream from the electron impact region we are able to detect fluorescence at 285 nm with the electron impact switched on and off. From the on-off fluorescence ratio at 285 nm we estimate that about 40% of the atoms exiting the oven are transferred to metastable states.

The 383-nm light is produced by frequency doubling of an external cavity diode laser (ECDL) operated at 766 nm. After passing through a 40-dB optical isolator, the 766-nm

light is injected into a tapered diode amplifier, resulting in an output of about 500 mW. The output of the tapered amplifier is directed through another 40-dB isolator and then coupled into a second-harmonic generation bow tie cavity. With a 5-mm antireflective coated bismuth triborate crystal (BiB₃O₆ or BIBO) we obtain an output of typically 65 mW at 383 nm.

A piezotransducer in the ECDL is used for scanning laser frequency over the entire scan range. Calibration of the frequency scan is achieved by modulating the AOM rf frequency with a known frequency of 15 MHz, thus generating two sidebands at ± 15 MHz relative to the carrier frequency, yielding a conversion factor κ , which relates the output laser frequency ν to the piezotransducer voltage U_{piezo} ($\kappa = d\nu/dU_{\text{piezo}}$). Repeated measurements at different levels of laser diode current reveal the conversion factor κ to be approximately linearly dependent on U_{piezo} , having a small positive slope. Over the scanned voltage range κ varies by $\pm 1.6\%$. All spectra have been corrected for this voltage dependency. We probe the metastable atoms using the first AOM order diffracted at 240 MHz. By chopping the AOM rf input at 45 kHz we achieve additional noise reduction in a phase-sensitive detection scheme with a lock-in amplifier.

Spectroscopy is performed at a distance of 45 cm from the oven orifice of $\varnothing 2$ mm using linearly polarized light. A $\varnothing 1$ -mm skimmer placed 25 cm from the oven orifice further reduces the transverse Doppler effect. The photomultiplier tube is located perpendicular to both the 383-nm laser beam and the metastable atom beam. Each spectrum is averaged over 20–22 scans.

Typically, the laser power was about 0.8 mW, resulting in a power broadening half-width at half maximum (HWHM) theoretically estimated to be 20 MHz for the ^{24}Mg isotope, which is confirmed experimentally by analysis of the measured spectra. In Table II we list theoretically estimated contributions from various broadening mechanisms associated with our experiment. The list includes residual Doppler effect, Zeeman broadening due to magnetic fields, power broadening, and transit time broadening. From Table II we see that Doppler and power broadenings are the main contributors. For this reason transit time broadening and the Zeeman effect, as well as differences in isotope mass, have been assumed negligible in the following analysis of the measured spectra.

Based on the geometry of the setup and the temperature of the oven we estimate a Doppler broadening HWHM of 17 MHz as stated in Table II. The calculation of the Doppler broadening assumes a shifted Maxwell-Boltzmann velocity distribution as given in Ref. [8] since interaction with the electrons in the discharge region has been observed to shift the

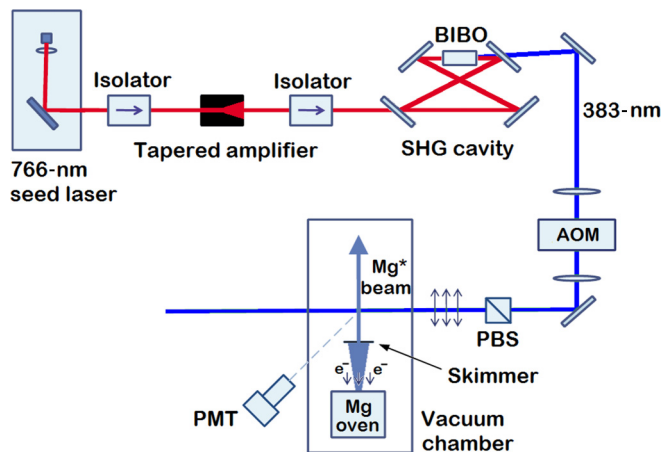


FIG. 2. (Color online) Schematic of the experimental system. The 383-nm light is provided by frequency doubling of a 766-nm external cavity diode laser in a bow tie cavity using a bismuth triborate (BIBO) crystal. Vertical polarization is assured by a polarizing beam splitter (PBS). A metastable magnesium beam is generated by electron impact and probed about 45 cm above the oven orifice after passing a $\varnothing 1$ -mm skimmer. The 383-nm light intersects the metastable beam at a right angle. Fluorescence detection is performed at right angles to the incoming laser beam and the metastable beam using a photomultiplier tube (PMT). The acousto-optic modulator (AOM) offers the possibility to perform spectroscopy with both zeroth and first orders as well as chopping the laser beam for phase-sensitive detection.

TABLE II. Estimated values for the broadening mechanisms associated with the experimental setup. All values are in megahertz.

Broadening effect	HWHM broadening
Doppler effect	17
Power broadening	20
Transit time broadening	0.5
Zeeman effect	0.7
Total	30

velocity distribution to higher values. However, the velocity distribution has not been measured for this particular oven, and the calculated Doppler broadening is thus only an estimate. From the measured spectra we extract a Doppler broadening value of about 22 MHz.

In total, the ^{24}Mg and ^{26}Mg peaks were observed to have HWHMs of 35 MHz. The ^{25}Mg transitions have lower transition dipole moments and thus lower absorption transition rates than ^{24}Mg and ^{26}Mg as detailed in Appendix B in (B14). The ^{25}Mg multiplet can thus be expected to have slightly narrower peaks as was confirmed experimentally with HWHM values in the range of 26–30 MHz.

V. RESULTS AND DISCUSSION

The measured spectra consist of the $^3P_0\text{--}^3D_1$ transition for the ^{24}Mg and ^{26}Mg isotopes as well as nine allowed $^3P_0\text{--}^3D_J$ hyperfine transitions of the ^{25}Mg isotope. We model the peaks of all three isotopes as Voigt profiles [19]. The extracted relative positions, relative amplitudes, and Lorentz widths of the 11 peaks fix the five independent reduced matrix elements of $\mathbf{T}^{(1)}$ and the isotope shifts $\Delta^{24\text{--}25}$ and $\Delta^{24\text{--}26}$, see Appendix B for details.

In Fig. 3 we show a fit of our model, detailed in Appendix B, to a typical experimental spectrum. From the model, the contribution of each transition can be identified. The $^3P_0\text{--}^3D_1$ peak is shown in black for ^{24}Mg and in red for ^{26}Mg , whereas the dipole allowed transitions from 3P_0 to the ^{25}Mg triplet D hyperfine levels are shown in green and labeled (a)–(h). Our model shows that three ^{25}Mg resonances are located below the large asymmetric peak of ^{24}Mg and ^{26}Mg . Furthermore, we observe five additional peaks, attributed to ^{25}Mg , which are clearly separated from the large asymmetric peak. Due to a small transition rate (10^{-3} times the ^{24}Mg transition rate) the ninth ^{25}Mg transition having $F = 3/2$ and located between (g) and (h) (at 799 MHz in Fig. 3 and at 553 MHz in Fig. 4 where

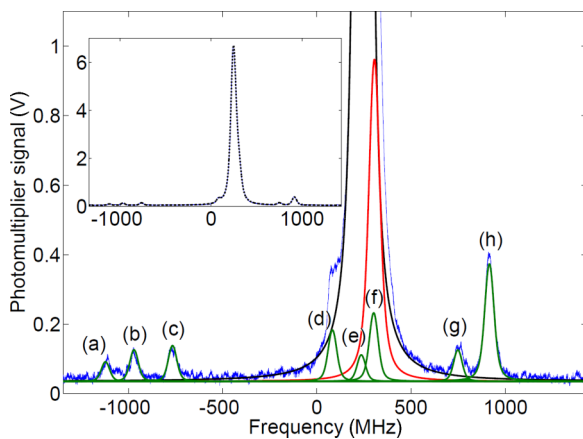


FIG. 3. (Color online) Fluorescence signal at 383 nm corresponding to the total $^3P_0\text{--}^3D_1$ multiplet (blue), the fitted model (dashed black, in the inset), and the 11 Voigt profiles that sum up to the fitted model. The individual Voigt profiles are the ^{24}Mg transition (black), the ^{26}Mg transition (red), and the nine allowed ^{25}Mg transitions (green). The labels (a)–(h) correspond to the labels given in Fig. 4. The midpoint of the scanning range is used as zero for the frequency axis.

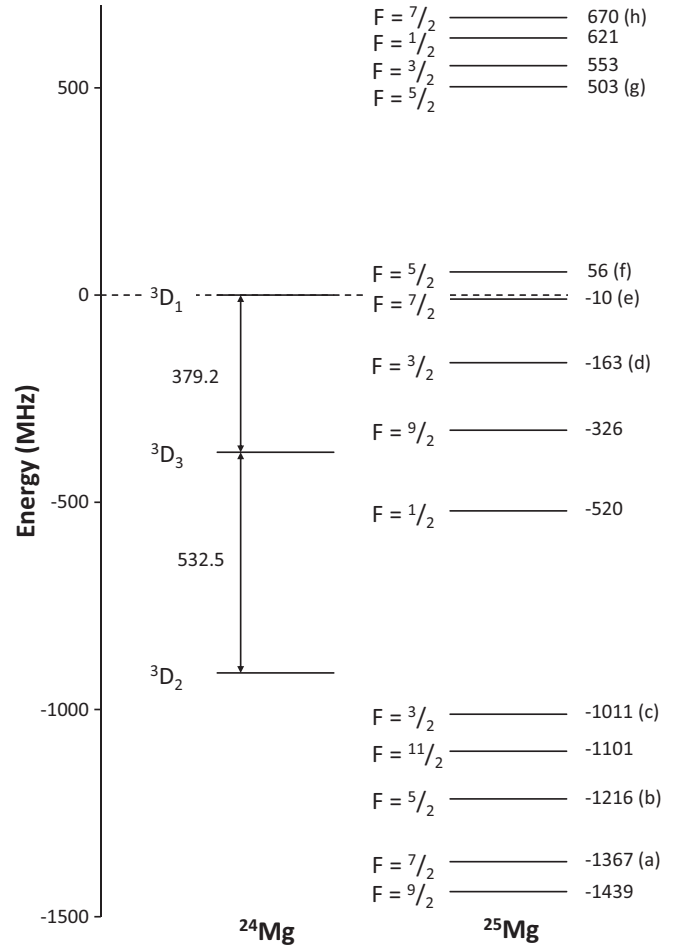


FIG. 4. The fine structure levels of the ^{24}Mg triplet D (values from Ref. [10]) and the hfs levels of the ^{25}Mg triplet D (this paper). The 3D_1 level of ^{24}Mg is used as zero for the energy axis, and the labels (a)–(h) correspond to the labels given in Fig. 3. All values are given in megahertz. Note that the number of significant figures does not correspond to the size of the error bars on the values for ^{25}Mg and that the value $\Delta^{24\text{--}25} = 6$ MHz has been used to calculate the energy levels.

^{24}Mg 3D_1 is used as zero) is not visible, although it is included in the model.

Based on the spectroscopic data we extract the five independent matrix elements $T_{JJ'} \equiv \langle ^3D_J || T^{(1)} || ^3D_{J'} \rangle$ and two isotope shifts $\Delta^{24\text{--}25}$ and $\Delta^{24\text{--}26}$. In Table III we show weighted averages where all energies are reported in megahertz. When solving the Schrödinger equation $H\Phi = E\Phi$, both Φ and $-\Phi$ are solutions. As a result, the model is indifferent to the signs of T_{12} and T_{23} , and only the absolute values of these have been stated in Table III. The statistical error bars are based on the fitting of the model. The dominant systematic error arises due to the statistical error on the mean value and slope of the voltage-dependent conversion factor κ introduced in Sec. IV. The noted systematic errors do not represent standard deviations but are estimates of the impact resulting from the statistical uncertainty on the conversion factor κ . By varying the mean and slope of κ within one standard deviation and repeating the fitting procedure, the dependencies of the fitted

TABLE III. Experimentally measured and theoretically calculated values of the reduced matrix elements $T_{JJ'} = \langle {}^3D_J \| T^{(1)} \| {}^3D_{J'} \rangle$ and experimental values of the isotope shifts Δ^{24-25} and Δ^{24-26} . The statistical errors σ_{stat} are the standard deviations for each experimental value. The systematic errors σ_{sys} correspond to the maximum effect on each experimental value of varying the conversion factor κ within one standard deviation. The calculated theoretical values have been obtained using the CI+all-order formalism. All values are in megahertz.

	Expt.	σ_{stat}	σ_{sys}	Theory
T_{11}	-1010	± 6	$\begin{smallmatrix} +48 \\ -47 \end{smallmatrix}$	-1025 ± 10
T_{22}	936	± 13	$\begin{smallmatrix} +97 \\ -97 \end{smallmatrix}$	773 ± 8
T_{33}	2597	± 21	$\begin{smallmatrix} +78 \\ -61 \end{smallmatrix}$	2567 ± 26
$ T_{12} $	1752	± 4	$\begin{smallmatrix} +58 \\ -56 \end{smallmatrix}$	1781 ± 18
$ T_{23} $	1657	± 9	$\begin{smallmatrix} +97 \\ -97 \end{smallmatrix}$	1812 ± 18
Δ^{24-25}	6	± 2	$\begin{smallmatrix} +9 \\ -8 \end{smallmatrix}$	
Δ^{24-26}	59.7	± 0.4	$\begin{smallmatrix} +0.4 \\ -0.4 \end{smallmatrix}$	

variables on κ are mapped out. The largest impact results from varying the mean value of κ , and the largest changes in the fitted variables occur when the upper and lower bounds of the mean are inserted. The resulting fitted values of the $T_{JJ'}$'s, Δ^{24-25} and Δ^{24-26} have been used as the upper and lower values of the systematic error bars.

We note from Table III that the experimental values of T_{11} , T_{33} , and T_{12} lie within one error bar of the theoretical values, whereas for T_{22} and T_{23} the differences are around 1.5 error bars, agreeing with the expectation that on average 68% of any set of measured values lies within the range of one standard deviation of the mean. However, in order to investigate the differences between measured and experimental T_{22} and T_{23} values, mixing between 1D_2 and 3D_2 has been investigated theoretically but proved unable to explain the differences.

The hfs constants $A({}^3D_J)$, calculated from the three diagonal elements T_{JJ} , are presented in Table IV. Theoretical values found using the CI+all-order formalism are also presented in both Table III and Table IV, see Sec. III for details. If we assume that only the $3s$ electron contributes to the hfs constants of the $3s3d^3D_J$ states (neglecting the contribution of the $3d$ electron), one can show [20] that a sum rule exists in this approximation, stating that $A({}^3D_1) + A({}^3D_2) + A({}^3D_3) = 0$. The measured hfs constants are observed to sum up to

TABLE IV. Experimentally measured and theoretically calculated values of the hfs constants $A({}^3D_J)$. The statistical and systematic errors σ_{stat} and σ_{sys} correspond to one standard deviation for each experimental value. The measured values have been obtained from the measured T_{JJ} of Table III, and the calculated values have been obtained using the CI+all-order formalism. All values are given in megahertz.

	Expt.	σ_{stat}	σ_{sys}	Theory
$A({}^3D_1)$	141	± 1	$\begin{smallmatrix} +7 \\ -7 \end{smallmatrix}$	143.3 ± 1.4
$A({}^3D_2)$	-59	± 1	$\begin{smallmatrix} +6 \\ -6 \end{smallmatrix}$	-48.3 ± 0.5
$A({}^3D_3)$	-97	± 1	$\begin{smallmatrix} +2 \\ -3 \end{smallmatrix}$	-96 ± 1

TABLE V. Measured ${}^{24}\text{Mg}$ - ${}^{25}\text{Mg}$ and ${}^{24}\text{Mg}$ - ${}^{26}\text{Mg}$ isotope shifts for the 3P_0 - 3D_1 transition reported by Hallstadius and Hansen [21] and Beverini *et al.* [9] compared to this paper. The statistical and systematic errors σ_{stat} and σ_{sys} are noted for each experimental value for this paper as in Table III. All values are in megahertz.

	Δ^{24-25}	Δ^{24-26}
Hallstadius and Hansen [21]	30	60
Beverini <i>et al.</i> [9]		65.0 ± 3
This paper	$6 \pm 2_{-8}^{+9}$	$59.7 \pm 0.4_{-0.4}^{+0.4}$

-15 MHz, which is around 1.5 times the standard deviation of the sum, whereas the theoretical values sum up to -1 MHz.

The isotope shifts Δ^{24-25} and Δ^{24-26} for the 3P_0 - 3D_1 transitions have been measured previously by Hallstadius and Hansen [21] and Beverini *et al.* [9]. For comparison, their results are listed in Table V along with the values found in this paper. Our values represent an improvement of the uncertainty by a factor of 6 compared to the best previous measurements of Δ^{24-26} . The value of Δ^{24-25} has proved difficult to measure [10,21,22]. The best measurement is by Hallstadius and Hansen [21], who measured a value of 30 MHz, but were unable to assign an error bar to that number. In this paper an error bar is assigned but is comparable in size to the quantity.

Based on the values of Table III, the 14 hyperfine energy levels of the ${}^{25}\text{Mg}$ triplet D can be estimated along with the composition of the hyperfine states. The positions of the ${}^{25}\text{Mg}$ hyperfine energy levels, relative to the fine structure levels of ${}^{24}\text{Mg}$, are shown in Fig. 4. In order to compare the levels of ${}^{24}\text{Mg}$ and ${}^{25}\text{Mg}$, all the energy levels are reported relative to the 3D_1 level of ${}^{24}\text{Mg}$. The value $\Delta^{24-25} = 6$ MHz of Table III has been used. Notice from the figure that the hyperfine energy levels of ${}^{25}\text{Mg}$ 3D_J are distributed over a range from -1500 to 700 MHz relative to 3D_1 of ${}^{24}\text{Mg}$ and that there are energy levels located both below and above the ${}^{24}\text{Mg}$ triplet D fine structure levels.

Knowing the energy levels of ${}^{25}\text{Mg}$ 3D_J and their compositions, it is possible to assign state labels to the transitions observed in the 3P_0 - 3D_1 spectrum. In Fig. 4 the ${}^{25}\text{Mg}$ levels involved in the 3P_0 - 3D_1 transitions have been labeled (a)-(h), and in Fig. 3 the transitions have been labeled correspondingly.

The 3P_0 - 3D_1 spectrum has been measured previously [9], but here state labels have been assigned to the transitions. Similarly, the transitions of the 3P_1 - ${}^3D_{1,2}$ and 3P_2 - ${}^3D_{1,2,3}$ spectra may be assigned state labels from knowledge of the 14 energy levels and their relative peak amplitudes. Of these, only the $({}^3P_2, F = 9/2) \rightarrow ({}^3D_3, F = 11/2)$ transition of the 3P_2 - ${}^3D_{1,2,3}$ multiplet has previously been assigned a state label [9]. However, the 3P_1 - ${}^3D_{1,2}$ and 3P_2 - ${}^3D_{1,2,3}$ multiplets are more crowded with allowed transitions than the 3P_0 - 3D_1 multiplet, and the errors on the calculated energy levels may prove too large to identify all the transitions in these spectra.

VI. CONCLUSION

In this paper we have analyzed the hyperfine structure of the ${}^{25}\text{Mg}$ $(3s3d)^3D_J$ levels through spectroscopy of the

$(3s3p)^3P_0$ - $(3s3d)^3D_1$ transition multiplet for the stable isotopes ^{24}Mg , ^{25}Mg , and ^{26}Mg , combined with theoretical calculations using the CI+all-order formalism. A comparable fine and hyperfine splitting of the ^{25}Mg triplet $(3s3d)^3D$ induces mixing between hyperfine levels of the same F , and the number of levels with nonzero projections onto $J = 1$ states is increased to nine. Taking this into account we have shown that the hyperfine structure Hamiltonian can be completely characterized in terms of five linearly independent reduced matrix elements of $\mathbf{T}^{(1)}$. Based on this we have developed a model relating the five matrix elements as well as the isotope shifts for ^{24}Mg , ^{25}Mg , and ^{26}Mg , to the line shape of the observed spectra.

By applying the developed model we have extracted all 14×14 matrix elements of the hyperfine structure Hamiltonian from experimental data and established the hyperfine coefficients $A(^3D_1) = 141 \pm 7$, $A(^3D_2) = -59 \pm 6$, and $A(^3D_3) = -97 \pm 3$ MHz. The hyperfine coefficients are in agreement with the state-of-the-art CI+all-order formalism predictions giving $A(^3D_1) = 143.3 \pm 1.4$, $A(^3D_2) = -48.3 \pm 0.5$, and $A(^3D_3) = -96 \pm 1$ MHz. In order to extract the hyperfine structure of the ^{25}Mg triplet $(3s3d)^3D$ from the measured spectra, the isotope shifts $\Delta^{24-25} = 6 \pm 9$ and $\Delta^{24-26} = 59.7 \pm 0.5$ MHz were also extracted, and the uncertainties on these values have been reduced significantly compared to previous measurements.

Experiments involving a magneto-optical trap (MOT) at 383 nm would enable a very clean spectroscopic signal to be derived. The MOT in this case is isotope sensitive [2] and would allow trapping and subsequent individual probing of the various magnesium isotopes. Refined measurements of the hyperfine structure of ^{25}Mg can thus be envisioned.

ACKNOWLEDGMENTS

We would like to acknowledge financial support from The Danish Council for Independent Research for Natural Sciences and the Carlsberg Foundation. The work of S.G.P. was supported, in part, by U.S. NSF Grant No. PHY-1212442. We are grateful to M. Kozlov for useful discussions.

APPENDIX A: MATRIX ELEMENTS OF THE HYPERFINE STRUCTURE

In the following we consider only the first term in the series (2) so that $H_{\text{HF}} = \mathbf{N}^{(1)} \cdot \mathbf{T}^{(1)}$. The hyperfine structure Hamiltonian will thus have the matrix elements,

$$\begin{aligned} \langle ^3D_J, F | H_{\text{HF}} | ^3D_{J'}, F \rangle &= (-1)^{I+J+F} \langle I \| N^{(1)} \| I \rangle \\ &\times \langle ^3D_J \| T^{(1)} \| ^3D_{J'} \rangle \begin{Bmatrix} I & I & 1 \\ J & J' & F \end{Bmatrix}. \end{aligned} \quad (\text{A1})$$

For $\mathbf{N}^{(1)}$ we choose $\mathbf{N}^{(1)} = \boldsymbol{\mu} / \mu_N$ so that $\mathbf{N}^{(1)}$ is dimensionless and $\mathbf{T}^{(1)}$ has the dimension of energy. Thus,

$$\langle I \| N^{(1)} \| I \rangle = \frac{1}{\mu_N} \langle I \| \boldsymbol{\mu} \| I \rangle. \quad (\text{A2})$$

Using the Wigner-Eckart theorem [11] the magnetic dipole moment $\boldsymbol{\mu}$ can be rewritten as

$$\begin{aligned} \boldsymbol{\mu} &= \begin{pmatrix} I & 1 & I \\ -I & 0 & I \end{pmatrix} \langle I \| \boldsymbol{\mu} \| I \rangle, \\ &= \sqrt{\frac{I}{(2I+1)(I+1)}} \langle I \| \boldsymbol{\mu} \| I \rangle, \end{aligned} \quad (\text{A3})$$

where in the second line the Wigner $3j$ -symbol is written explicitly. Inserting the expression for $\boldsymbol{\mu}$ into (A2), we obtain

$$\langle I \| N^{(1)} \| I \rangle = \sqrt{\frac{(2I+1)(I+1)}{I}} \frac{\boldsymbol{\mu}}{\mu_N}. \quad (\text{A4})$$

For ^{25}Mg , the nuclear spin is $I = 5/2$, and the magnetic dipole moment is known from experiments to be $\boldsymbol{\mu} = -0.85546 \mu_N$ [23], and thus $\langle I \| N^{(1)} \| I \rangle = -2.47936$ is a known quantity.

The nine reduced matrix elements of $\mathbf{T}^{(1)}$ on the other hand are unknown. However, by insertion of $J = 1, 2, 3$ into (A1) it is seen that the coefficients of $\langle ^3D_1 \| T^{(1)} \| ^3D_3 \rangle$ and $\langle ^3D_3 \| T^{(1)} \| ^3D_1 \rangle$ are zero and that

$$\langle ^3D_1 \| T^{(1)} \| ^3D_2 \rangle = -\langle ^3D_2 \| T^{(1)} \| ^3D_1 \rangle, \quad (\text{A5})$$

$$\langle ^3D_2 \| T^{(1)} \| ^3D_3 \rangle = -\langle ^3D_3 \| T^{(1)} \| ^3D_2 \rangle. \quad (\text{A6})$$

Thus, only five of the 3×3 matrix elements are linearly independent, and H_{HF} may be specified by the five linearly independent reduced matrix elements of $\mathbf{T}^{(1)}$.

Now, consider the diagonal elements of (A1). Writing the Wigner $6j$ -symbol of (A1) explicitly and inserting (A4) we find

$$\begin{aligned} \langle ^3D_J, F | H_{\text{HF}} | ^3D_J, F \rangle &= \frac{1}{2I} \frac{\boldsymbol{\mu}}{\mu_N} \frac{\langle ^3D_J \| T^{(1)} \| ^3D_J \rangle}{\sqrt{J(J+1)(2J+1)}} \\ &\times [F(F+1) - I(I+1) - J(J+1)]. \end{aligned} \quad (\text{A7})$$

We recognize this as the usual expression for the diagonal matrix elements of the hyperfine structure Hamiltonian,

$$\begin{aligned} \langle ^3D_J, F | H_{\text{HF}} | ^3D_J, F \rangle &= \frac{A(^3D_J)}{2} [F(F+1) - I(I+1) - J(J+1)], \end{aligned} \quad (\text{A8})$$

and by inspection, the hfs constants are identified as

$$A(^3D_J) = \frac{\boldsymbol{\mu}}{\mu_N I} \frac{\langle ^3D_J \| T^{(1)} \| ^3D_J \rangle}{\sqrt{J(J+1)(2J+1)}}. \quad (\text{A9})$$

Thus, the hfs constants $A(^3D_J)$ can be expressed in terms of the diagonal matrix elements of $\mathbf{T}^{(1)}$.

APPENDIX B: THE FITTED MODEL

The Voigt profile describing each peak in the observed spectra is given by [19]

$$V(x, y) = A \frac{y}{\pi} \int_{-\infty}^{\infty} \frac{\exp(-u^2)}{y^2 + (x-u)^2} du, \quad (\text{B1})$$

where

$$y = \sqrt{\ln 2} \frac{\alpha_L}{\alpha_D} \quad \text{and} \quad x = \sqrt{\ln 2} \frac{\nu - \nu_0}{\alpha_D}, \quad (\text{B2})$$

with A being an amplitude prefactor, ν being the laser frequency, ν_0 being the peak center frequency, and α_L and α_D being the Lorentz and Doppler HWHMs, respectively. Summing up the profiles for each of the 11 allowed transitions we arrive at a model for the spectrum,

$$U(\nu) = U_0 + \sum_{j=24,25,26} \sum_i A_i^{(j)} \times V \left(\sqrt{\ln 2} \frac{\nu - \nu_i^{(j)}}{\alpha_D}, \sqrt{\ln 2} \frac{\alpha_{L,i}^{(j)}}{\alpha_D} \right), \quad (\text{B3})$$

where a vertical offset U_0 has been included. In this notation, the peak corresponding to the i th level of the j th isotope ${}^j\text{Mg}$ has the amplitude $A_i^{(j)}$, the center frequency $\nu_i^{(j)}$, the Lorentz width $\alpha_{L,i}^{(j)}$, and the Doppler width α_D . The mass differences between the isotopes are assumed negligible, and the velocity distributions are assumed identical for the three isotopes. As a result, the Doppler width α_D is assumed to have the same value for all peaks in the spectrum.

The parameters α_D and U_0 are fitted directly from each spectrum, whereas the remaining parameters $\nu_i^{(j)}$, $\alpha_{L,i}^{(j)}$, and $A_i^{(j)}$ are related to other parameters fitted from the spectra—among these the five linearly independent reduced matrix elements of $\mathbf{T}^{(1)}$ and the isotope shifts Δ^{24-25} and Δ^{24-26} . As a result, each spectrum can be described by only 12 fitted parameters.

1. Center frequency $\nu_i^{(j)}$

In each iteration of the fitting procedure the Hamiltonian (1) is calculated from the five linearly independent reduced matrix elements of $\mathbf{T}^{(1)}$. See Appendix A for details. Diagonalizing H we find the 14 eigenvalues $E_i^{(25)}$ and eigenstates $|\beta_i\rangle$ that each can be written as

$$|\beta_i\rangle = \sum_{J=1,2,3} c_{J,i} |{}^3D_J, F\rangle, \quad (\text{B4})$$

where $c_{J,i} = \langle {}^3D_J, F | \beta_i \rangle$. Of the 14 eigenstates only 9 have nonzero projections $c_{1,i}$ onto states with $J = 1$.

The spectra of ${}^{25}\text{Mg}$ and ${}^{26}\text{Mg}$ are shifted relative to the ${}^{24}\text{Mg}$ energy level $E^{(24)}$ by the isotope shifts Δ^{24-25} and Δ^{24-26} , respectively, and the center frequencies of the transitions are thus,

$$h\nu^{(24)} = E^{(24)}, \quad (\text{B5})$$

$$h\nu^{(26)} = E^{(24)} + \Delta^{24-26}, \quad (\text{B6})$$

$$h\nu_i^{(25)} = E^{(24)} + \Delta^{24-25} + E_i^{(25)}, \quad (\text{B7})$$

where $E^{(24)}$, Δ^{24-25} , and Δ^{24-26} are fitted from each spectrum, alongside the five linearly independent reduced matrix elements of $\mathbf{T}^{(1)}$ necessary for the calculation of $E_i^{(25)}$.

2. Lorentz width $\alpha_{L,i}^{(j)}$

A transition experiencing power broadening has the Lorentzian HWHM of [24]

$$\alpha_L = \frac{\Gamma}{4\pi} \left(1 + \frac{2\Omega^2}{\Gamma^2} \right)^{1/2}, \quad (\text{B8})$$

where Γ and Ω are the natural linewidth (FWHM) and the Rabi frequency of the transition, respectively. The Rabi frequency can be related to the transition dipole moment, which again can be related to the line strength of the transition. Using a general result of Ref. [11] about transition line strengths, it can be shown that

$$\Omega^2 = \frac{E_0^2}{\hbar^2} (2F + 1) \begin{Bmatrix} J & F & I \\ F' & J' & 1 \end{Bmatrix}^2 S(\gamma J; \gamma' J'), \quad (\text{B9})$$

where E_0 is the electric field amplitude and S is the line strength. Primed and unprimed quantum numbers refer to the final and initial states of the transition, respectively. Inserting into (B8) we arrive at an expression for the Lorentz width of each transition,

$$\alpha_{L,i}^{(j)} = \frac{\Gamma}{4\pi} (1 + |c_{1,i}|^2 \eta_i C)^{1/2}, \quad (\text{B10})$$

where $c_{1,i}$ are the projection coefficients of (B4), whereas C and η_i are defined as

$$C = \frac{4}{\epsilon_0 c \hbar^2 \Gamma^2} I_\nu S(\gamma J; \gamma' J'), \quad (\text{B11})$$

$$\eta_i = (2F' + 1) \begin{Bmatrix} J & F & I \\ F' & J' & 1 \end{Bmatrix}^2. \quad (\text{B12})$$

Here, $I_\nu = \frac{1}{2} \epsilon_0 c E_0^2$ is the laser light intensity. The parameter C is a constant of the transition whereas η_i is a dimensionless parameter dependent on the initial and final states. C is fitted from each spectrum, and $\alpha_{L,i}^{(j)}$'s are calculated from C .

3. Amplitude $A_i^{(j)}$

Now, we need only to obtain the amplitudes $A_i^{(j)}$ of the transitions to have expressions for all the elements of $U(\nu)$ in (B3). In the dipole approximation, the absorption transition rate for linearly polarized light from an energy level $|a\rangle$ to a higher-lying energy level $|b\rangle$ is given by [25]

$$W_{ba} = \frac{1}{4\pi \epsilon_0} \frac{4\pi^2}{c \hbar^2} I_\nu D_{ba}^2, \quad (\text{B13})$$

where D_{ba}^2 is the transition dipole moment. The transition dipole moment can be related to the line strength of the transition, and for the 3P_0 - 3D_1 transitions it can be shown that

$$W_{ba} = |c_{1,i}|^2 \eta_i K, \quad (\text{B14})$$

where K is defined as

$$K = \frac{1}{4\pi \epsilon_0} \frac{4\pi^2}{c \hbar^2} I_\nu S(\gamma J; \gamma' J'). \quad (\text{B15})$$

The transition amplitudes $A_i^{(j)}$ are proportional to both the transition rate W_{ba} , the natural abundance $N^{(j)}$ of the isotope

in question, and the electron excitation cross section for the isotope. To account for this, $A_i^{(j)}$ is calculated as

$$A_i^{(j)} = |c_{1,i}|^2 \eta_i N_{\text{dev}}^{(j)} N^{(j)} K, \quad (\text{B16})$$

where $N_{\text{dev}}^{(j)}$ accounts for the differences in electron excitation cross sections and is set equal to 1 for ^{24}Mg . K is fitted from each spectrum, and $A_i^{(j)}$'s are calculated using K .

To simplify the fitting procedure, $N_{\text{dev}}^{(26)}$ is fixed at the known value of 1.04 [26]. Fitting $N_{\text{dev}}^{(25)}$, or varying it in the range

from 0.9 to 1.1, was observed only to change the values of the other fitted variables by values smaller than their respective statistical uncertainties. For that reason $N_{\text{dev}}^{(25)}$ was fixed at unity.

To summarize, the 12 variables fitted from each spectrum are as follows: The five linearly independent ($\langle {}^3D_J \| T^{(1)} \| {}^3D_{J'} \rangle$), Δ^{24-25} , Δ^{24-26} , α_D , U_0 , $E^{(24)}$, C , and K . Of the 12, the first 7 parameters represent general properties of magnesium whereas the last 5 are dependent on the experimental setup.

-
- [1] A. J. Daley, J. Ye, and P. Zoller, *Eur. Phys. J. D* **65**, 207 (2011).
- [2] M. Riedmann, H. Kelkar, T. Wübbena, A. Pape, A. Kulosa, K. Zipfel, D. Fim, S. Rühmann, J. Friebe, W. Ertmer, and E. Rasel, *Phys. Rev. A* **86**, 043416 (2012).
- [3] B. J. Bloom, T. L. Nicholson, J. R. Williams, S. L. Campbell, M. Bishof, X. Zhang, W. Zhang, S. L. Bromley, and J. Ye, *Nature (London)* **506**, 71 (2014).
- [4] R. Le Targat, L. Lorini, Y. Le Coq, M. Zawada, J. Guéna, M. Abgrall, M. Gurov, P. Rosenbusch, D. G. Rovera, B. Nagórny, R. Gartman, P. G. Westergaard, M. E. Tobar, M. Lours, G. Santarelli, A. Clairon, S. Bize, P. Laurent, P. Lemonde, and J. Lodewyck, *Nat. Commun.* **4**, 2109 (2013).
- [5] T. Middelmann, S. Falke, C. Lisdat, and U. Sterr, *Phys. Rev. Lett.* **109**, 263004 (2012).
- [6] N. Hinkley, J. A. Sherman, N. B. Phillips, M. Schioppo, N. D. Lemke, K. Beloy, M. Pizzocaro, C. W. Oates, and A. D. Ludlow, *Science* **341**, 1215 (2013).
- [7] A. Lurio, *Phys. Rev.* **126**, 1768 (1962).
- [8] G. Giusfredi, A. Godone, E. Bava, and C. Novero, *J. Appl. Phys.* **63**, 1279 (1988).
- [9] N. Beverini, G. L. Genovesi, E. Maccioni, M. M. Messina, and F. Strumia, *Appl. Phys. B* **59**, 321 (1994).
- [10] K. W. Meißner, *Ann. Phys. (Leipzig)*, **423**, 505 (1938).
- [11] I. I. Sobelman, *Atomic Spectra and Radiative Transitions* (Springer-Verlag, Berlin, 1979).
- [12] S. G. Porsev, M. S. Safronova, and M. G. Kozlov, *Phys. Rev. A* **85**, 062517 (2012).
- [13] V. A. Dzuba, V. V. Flambaum, and M. G. Kozlov, *Phys. Rev. A* **54**, 3948 (1996).
- [14] M. S. Safronova, M. G. Kozlov, W. R. Johnson, and D. Jiang, *Phys. Rev. A* **80**, 012516 (2009).
- [15] M. S. Safronova, S. G. Porsev, M. G. Kozlov, and C. W. Clark, *Phys. Rev. A* **85**, 052506 (2012).
- [16] M. G. Kozlov, S. G. Porsev, and I. I. Tupitsyn, [arXiv:physics/0004076](https://arxiv.org/abs/physics/0004076).
- [17] S. A. Kotochigova and I. I. Tupitsyn, *J. Phys. B* **20**, 4759 (1987).
- [18] M. G. Kozlov, S. G. Porsev, V. A. Dzuba, and V. V. Flambaum, *Zh. Eksp. Teor. Fiz.* **114**, 1636 (1998) [*JETP* **87**, 885 (1998)].
- [19] B. H. Armstrong, *J. Quant. Spectrosc. Radiat. Transfer* **7**, 61 (1967).
- [20] H. Kopfermann, *Nuclear Moments* (Academic, New York, 1958).
- [21] L. Hallstadius and J. E. Hansen, *Z. Phys. A* **285**, 365 (1978).
- [22] H. Westmeyer, *Z. Phys.* **94**, 590 (1935).
- [23] P. Raghavan, *At. Data Nucl. Data Tables* **42**, 189 (1989).
- [24] C. J. Foot, *Atomic Physics* (Oxford University Press, Oxford, 2005).
- [25] B. H. Bransden and C. J. Joachain, *Physics of Atoms and Molecules* (Longman, London, 1983).
- [26] K. T. Therkildsen, Ph.D. thesis, Niels Bohr Institute, University of Copenhagen, 2009.